JOURNAL OF GEOPHYSICAL RESEARCH, VOL. 106, NO. A12, PAGES 28,913–28,924, DECEMBER 1, 2001

On the winding of auroral spirals: Interhemispheric observations and Hallinan's theory revisited

N. Partamies

Finnish Meteorological Institute, Geophysical Research, Helsinki, Finland
Department of Physics, University of Helsinki, Helsinki, Finland

M. P. Freeman

British Antarctic Survey, Cambridge, England

K. Kauristie

Finnish Meteorological Institute, Geophysical Research, Helsinki, Finland

Abstract. Auroral spirals are the largest vortex structures that appear in auroral arcs. Their diameters vary from tens to hundreds of kilometers. We have collected an all-sky camera data set of 216 events including 189 northern and 27 southern hemispheric spirals. For the first time in the literature, this study shows spiral structures from both hemispheres with similar occurrence distributions for their scale sizes and a sense of rotation that is always counterclockwise when viewed along the geomagnetic field. In a few cases the time resolution was adequate to follow the winding process and the relative brightness of the spirals. These events show that the winding motion of the auroral structure is opposite to the anticipated plasma flow in the same region, and that the winding process is controlled by the intensity of the auroral precipitation. We show that these findings are consistent with the model of *Hallinan* [1976]. He suggested that spirals are related to periodic undulations developing in an upward field-aligned current (FAC) sheet. In this model, the winding of the auroral structure manifests the magnetic field line twisting in a direction different from the ionospheric plasma flow. We discuss Hallinan's theory in more detail: First, we derive the complete solutions of the magnetic field perturbation. Second, we compute the structure of the FAC sheet and show that it reproduces the shape and sense of rotation of auroral spirals. Third, we consider the factors that affect the amount of spiral winding. In particular, we show that the spiral winding is controlled by the strength of the FAC perturbation in the arc and thereby is related to auroral precipitation and arc brightness observed. We also find the relationship between the finite field-aligned distance required for spirals to fully evolve and the amplitude of the FAC perturbation and discuss how this relationship could be used to identify the source region for the FAC perturbation. However, the assumption of a constant background field in the model hampers detailed comparisons with observed FACs and spatial scale sizes. Further development of the model is needed before we can conclude, for example, if at the altitude of the acceleration region, the conditions would be favorable for the spiral winding mechanism.

1. Introduction

Distortions in auroral arcs occasionally appear as vortical structures known as either curls, folds, or spirals. Curls are small and transient vortices with intercurl separations and diameters of less than 10 km and lifetimes of less than 2 s [*Hallinan and Davis,* 1970; *Trondsen and Cogger,* 1998]. Spirals are larger and more stable vortices with diameters of 20–1300 km, interspiral separations of the order of 100 km and lifetimes of up to 30 min [*Davis and Hallinan,* 1976; *Partamies et al.,* 2001]. Also, spirals occur preferentially in the morning and during quiet geomagnetic conditions [*Partamies et al.,* 2001]. Folds are less well-developed vortices of intermediate scale with interfold separations of 10–50 km

Copyright 2001 by the American Geophysical Union.

Paper number 2001JA900093..
0148-0227/01/2001JA900093$09.00

and lifetimes from seconds to a minute [*Hallinan and Davis,* 1970].

Besides the spatial and temporal scales, the key distinguishing parameter between curls and spirals or folds is the sense of rotation of the vortices. It is also an important parameter when considering the mechanism causing such structures. In the Northern Hemisphere the sense of rotation when viewed from above (the viewing direction used throughout the paper unless otherwise mentioned) is clockwise for curls [*Hallinan and Davis,* 1970] and counterclockwise for folds [*Hallinan and Davis,* 1970] and spirals [*Davis and Hallinan,* 1976]. In the Southern Hemisphere the sense of rotation is counterclockwise for curls [*Hallinan and Davis,* 1970] and clockwise for folds [*Hallinan and Davis,* 1970].

The winding dynamics of auroral vortices have also been analyzed. *Oguti* [1974] suggested that all vortices that are formed by a splitting of an auroral arc wind up clockwise, no matter what their scale size is. Furthermore, *Nakamura et al.* [1993] concluded that the counterclockwise vortex of the head of the westward traveling surge develops in a clockwise sense according to all-sky TV camera data. Assuming a region of upward field-aligned current (FAC) within the surge, there is also a converging electric field (and Pedersen currents) at the ionospheric foot point of the FAC. Thus in the Northern Hemisphere the corresponding $\mathbf{E} \times \mathbf{B}$ drift is clockwise, and the observations by Oguti and Nakamura et al. suggest the vortex winding along the anticipated plasma flow. However, the observations by *Samson et al.* [1996] (and references therein) show counterclockwise winding of large vortices, that is direction opposite to the plasma flow, although their theory predicts both winding directions.

Hallinan [1976] introduced a theoretical model to explain the spiral observations by *Davis and Hallinan* [1976]. In this model the auroral arc is associated with an upward FAC sheet, and the spiral is a product of an instability due to magnetic shear caused by an enhanced field-aligned current filament. The extra azimuthal magnetic field of the filament then bends the sheet. At the magnetospheric end the distortion is small but grows as it propagates along the field lines, so that at the ionospheric end the current sheet forms a spiral. The instability is analogous to the Kelvin-Helmholtz instability (KHI) due to velocity shear but with field-aligned current playing the role of fluid vorticity. *Hallinan and Davis* [1970] argued that the KHI itself was the mechanism for generation to auroral curls. This argument seems to be supported by recent simulations of the KHI in field line resonances that produce vortices of the order of 10 km scale that wind in a clockwise sense [*Voronkov et al.,* 1999].

In this paper we present both new observations in section 2 and a new insight into Hallinan's theory in section 3: We show comparable observations from both hemispheres that agree with Hallinan's predicted winding directions of the spirals. The similarity of the statistics of the spiral sizes confirms that the definition of the spirals (see the first paragraph of this section) applies in both hemispheres and that we have observed the same phenomenon. To the best of our knowledge, this study presents the first southern hemispheric spiral observations with explicit spatial scale estimations. Also, we strive to combine the changes in spiral brightness during the winding process in a more reliable way than they have been measured before. In addition, we aim to combine the theory and the observations qualitatively as closely as possible, by investigating the complete solution of Hallinan's theory for the magnetic field and the structure of the auroral spiral current sheet. Sections 4 and 5 contain the discussion and conclusions, respectively.

2. Observations

2.1. Instrumentation and Data Description

In this study we used recordings of six all-sky cameras (ASC) of the Magnetometers – Ionospheric Radars – All-sky Cameras Large Experiment (MIRACLE) network [*Syrjäsuo et al.,* 1998] in the Northern Hemisphere and one ASC in the Southern Hemisphere. The MIRACLE ASC stations are located between 64.6° and 75.1° corrected magnetic latitude (CGM), in northern Fennoscandia and on Svalbard. These cameras take filtered images (λ = 557.7nm) once every 20 s. Their field-of-view (fov) at the altitude of 110 km is a circle with the diameter of about 600 km (corresponding to a fov of 140° and a square of 440 × 440 pixels). The spatial resolution of an ASC image depends on the elevation angle. The average resolution is about 600 km / 440 pixels = 1.4 km / pixel, but at the edge of the image it is still better than 10 km / pixel.

The TULA ASC at Halley base (75°36'S and 26°19'W) in the Antarctic takes white light images once every minute. The diameter of the camera fov is about the same as that of the MIRACLE cameras, while the spatial resolution is lower (168 × 192 pixels in the image). The geomagnetic latitude of Halley is -61.6°, and thus the station is located somewhat equatorward of the main auroral zone.

2.2. Interhemispheric Comparisons

ASC images from the northern winters of 1996–1998 contain 189 spiral forms, whereas in the recordings from the southern winters of 1996–1998 we found 27 spirals. Figure 1 shows the diameter distributions of the northern and southern hemispheric spiral forms. The peak value of the diameter distributions is the same, and their ranges are similar, too. The absence of southern spirals with diameters less than 25 km is due to the lower resolution of the ASC at Halley. The histograms in Figure 1 confirm that we are dealing with the same phenomenon in both hemispheres.

Example images in Plate 1 show the direction of the spiral winding in the two hemispheres. On the left-hand

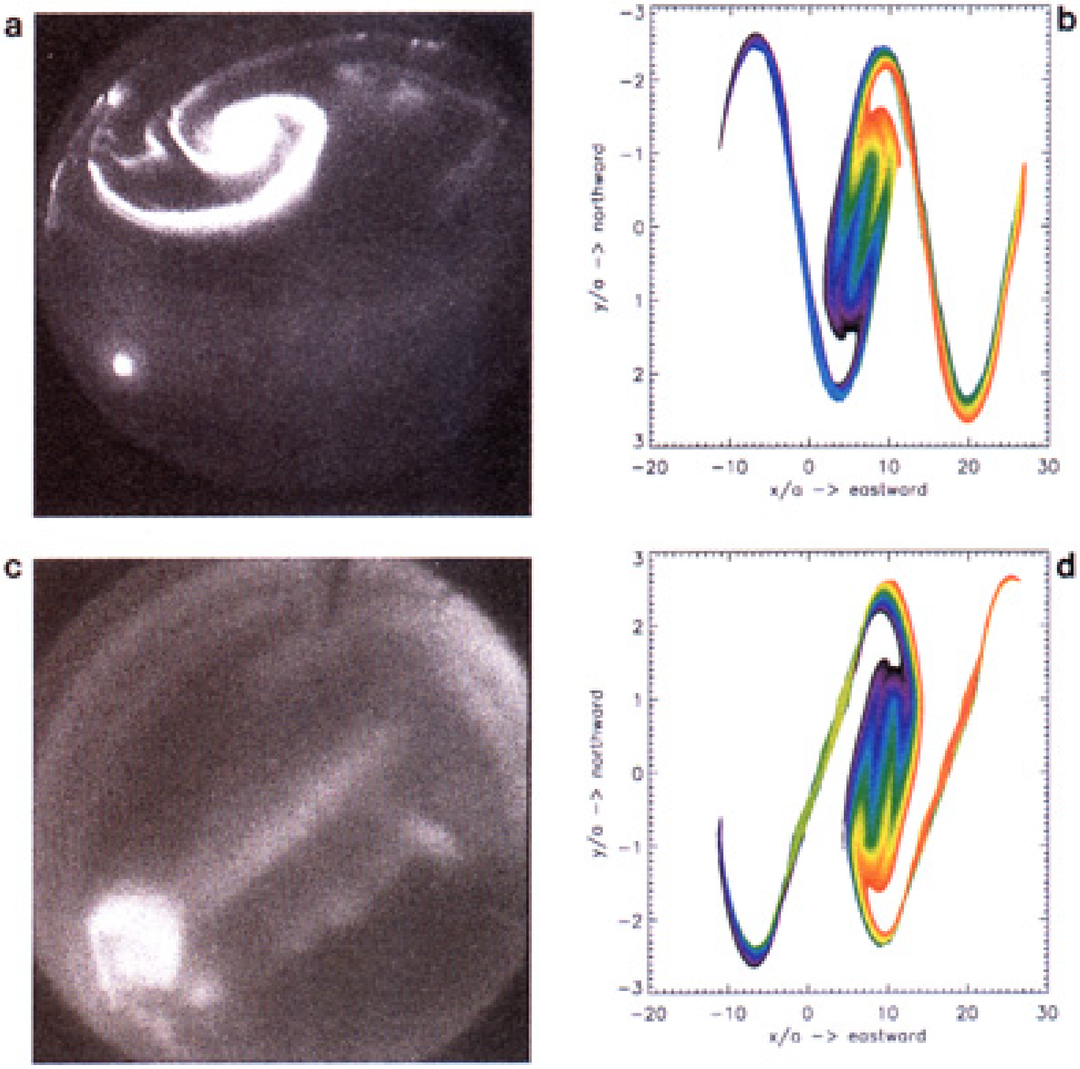

Plate 1. An example of the spiral winding viewed along the geomagnetic field, observations on the left and model on the right. The northern hemispheric spiral is in Plate 1a (Kilpisjärvi, March 22 1997 at 00:41:40 UT) and the southern hemispheric structure in Plate 1c (Halley, April 24 1998 at 01:46:00 UT). For the modeled spirals, $k^* = 0.4$ is chosen to give the maximum growth (γ^*) along the field line. North is on the top, south on the bottom, east on the right, and west on the left of each image.

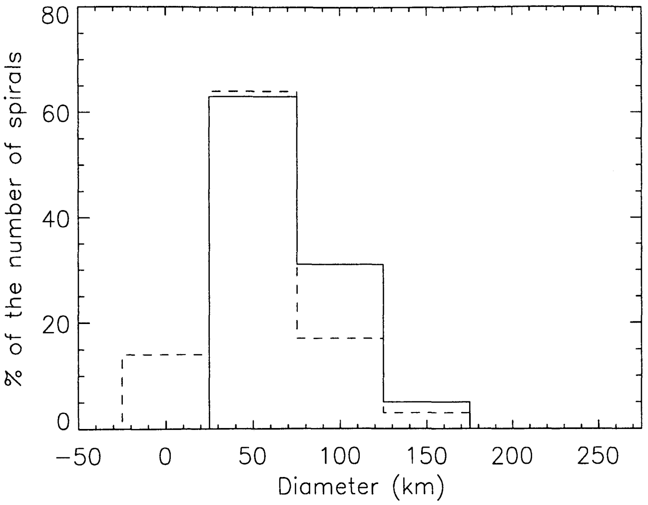

Figure 1. Diameter distribution of the southern (solid) and the northern (dashed) spirals.

side there are the actual ASC images: a spiral observed at Kilpisjärvi in the Plate 1a and a spiral recorded at Halley in the Plate 1c. The viewing direction is from above. The southern hemispheric spiral is a mirror image of the northern hemispheric spiral. In all cases the winding direction of the structures is systematically consistent with the prediction by *Hallinan* [1976]: counterclockwise in the Northern Hemisphere and clockwise in the Southern Hemisphere when viewed from above. Plates 1b and 1d show the northern and southern spirals, respectively, according to the model by *Hallinan* [1976] and will be discussed in more detail in section 3.

2.3. Temporal Development

Eight consecutive ASC images in the second and fourth rows of Figure 2 represent an example of the temporal development of a spiral. This spiral was observed in Kilpisjärvi on March 22, 1997. The image interval is 20 s, which in this case appears to be just enough to follow the spiral evolution. The spiral winds up and unwinds twice during the 160 s time period shown here, and after the last included image the structure fades away. Both windings result from counterclockwise motion (from the second to third image and from the fourth to fifth image) of the spiral structure, while the following unwindings perform clockwise rotations of the aurora (from the third to fourth image and from the fifth to sixth image). This behavior is different from that reported by *Nakamura et al.* [1993]. Their TV recordings have shown that the development of a surge does not always obey the same sense of rotation as the final structure shows. Especially, westward traveling surges, which occasionally resemble large spirals, may develop as a consequence of clockwise motion of auroral structures.

The changes in the auroral spiral luminosity can be estimated by using the relative intensity units of the ASC images, in which the intensity of each pixel is linearly scaled to cover the range from 0 to 255 units. The sum of the relative intensity values within the ASC fov is marked as asterisks in the middle panel of Figure 2. This curve shows that the summed intensity increases when the loop drifts into the fov (00:41:00 to 00:41:20) and when the spiral winds up (00:41:20 to 00:41:40), stays almost constant during the unwinding and rewinding of the spiral (00:41:40 to 00:42:20), and finally starts to decrease when the spiral unwinds again (00:42:40 to 00:44:00). The diamonds in Figure 2 represent the number of saturated pixels (relative intensity, 255) in the corresponding images. These values vary similarly to the summed intensities, except that they peak more clearly at both windings (in the third and fifth images), and thus show a relation between the winding and brightening (unwinding and dimming) of the spiral. The intensity in the ASC image depends on the zenith angle of the observed structure. However, from the third image onward, we believe this to be a minor effect in our case here, because the zenith angle of the spiral remains almost constant. *Moen et al.* [1994] reported similar variations in the absolute luminosity values during the winding of a spiral. The absolute brightness in their study was recorded by a narrow track of a meridionally scanning photometer that crossed the spiral. Thus our summed intensities based on ASC images with a better spatial coverage (and thus less sensitive for possible spiral drift motions) confirm the conclusion of *Moen et al.* [1994].

The connection between the winding process and auroral brightness is easily seen in ASC animations, but its rigorous documentation is only occasionally possible. To prove this relation, we examined the relative intensities during the evolution of an arc to a fully evolved spiral for nine more events, where neither the fast motion, short lifetime nor bad location (too far from the zenith) of the structure complicated the interpretation. Plotted in Figure 3 are the sums of the relative intensities (normalized by their maximum value and scaled to the same starting point) during the spiral winding as a function of time (normalized by the whole evolution time, here 40–80 s). Figure 3 clearly demonstrates how in all of the analyzed cases the aurora brightened during the winding process.

3. A Theoretical Model of Spiral Formation by KH-Type Instability

3.1. Derivation in a General Form

Here, we develop the auroral spiral theory of *Hallinan* [1976] to derive the complete solutions for the magnetic field twisting due to a perturbed current sheet and hence model the auroral spiral. The Cartesian coordinate system we use in this paper is shown in Figure 4. In this coordinate system the plane $z = 0$ corresponds to the magnetospheric equator, and $z = z_{\text{lim}}$ and $z = -z_{\text{lim}}$ refer to the northern and southern ionospheres, respectively. Thus the positive z direction is

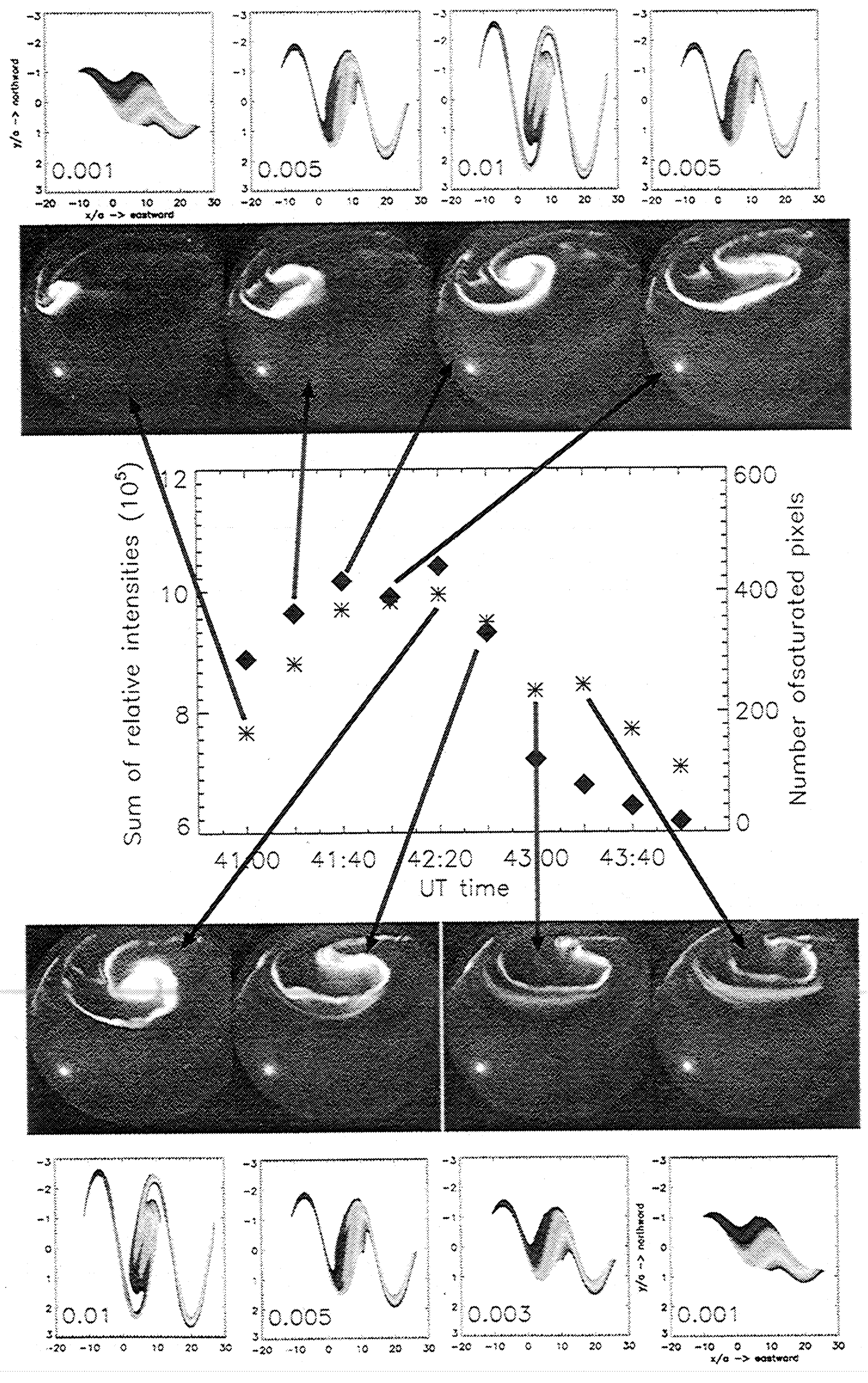

Figure 2. An example of evolution of a spiral. The second and fourth rows show eight successive all-sky camera images of a spiral. The middle row shows the sum of the relative intensity of the all-sky images (asterisks) together with the number of saturated pixels (diamonds). The uppermost and lowermost panels show similar quasi-periodic variation of the model spiral due to changes in C_1^* between 0.001 and 0.1.

from the southern to the northern ionosphere, and the x axis points eastward. The y direction completes the right-handed coordinate system. The FAC sheet is chosen to be in the x–z plane, and its width is $2a$. The magnetic field consists of three parts: the background field $B_{0z}(y)$, the field related to the FAC sheet $B_{0x}(y)$, and the perturbation field caused by the enhanced FAC filament $\mathbf{B_1}(x, y, z)$. According to Ampère's law

$$\begin{cases} \mu_0 j_{0x} = \frac{\partial B_{0z}}{\partial y} \\ \mu_0 j_{0y} = 0 \\ \mu_0 j_{0z} = -\frac{\partial B_{0x}}{\partial y} \end{cases} \tag{1}$$

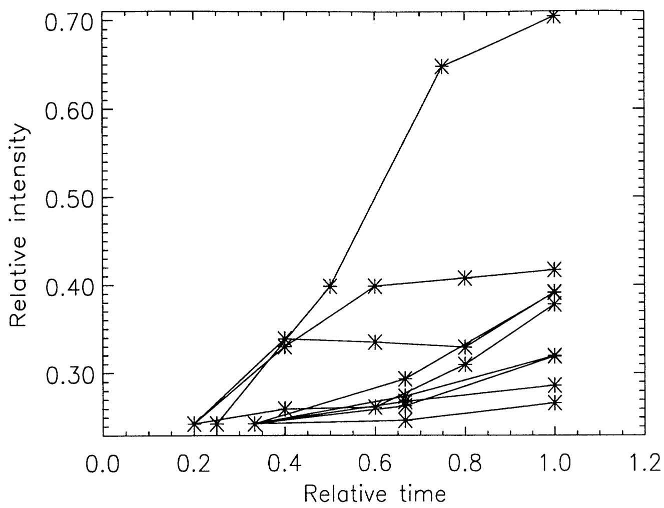

Figure 3. Variation of the relative intensity of the spiral during the winding process. The asterisks mark the intensity values of the separate all-sky camera (ASC) images, and the curves show the intensity changes as a function of time (normalized).

where j_0 is the current density in the FAC sheet. Adding a small perturbation (subscript 1) to the background (subscript 0) magnetic field $\mathbf{B} = \mathbf{B_0} + \mathbf{B_1}$, thermal pressure $p = p_0 + p_1$, and current density $\mathbf{j} = \mathbf{j_0} + \mathbf{j_1}$, we obtain a new solution for the perturbation fields:

$$\begin{cases} \mu_0 j_{1x} = \frac{\partial B_{1z}}{\partial y} - \frac{\partial B_{1y}}{\partial z} \\ \mu_0 j_{1y} = \frac{\partial B_{1x}}{\partial z} - \frac{\partial B_{1z}}{\partial x} \\ \mu_0 j_{1z} = \frac{\partial B_{1y}}{\partial x} - \frac{\partial B_{1x}}{\partial y} \end{cases} \tag{2}$$

By applying the balance between the $\mathbf{J} \times \mathbf{B}$ force and the thermal pressure gradient ∇p we get (when $B_{0y} = j_{0y} = 0$)

$$\begin{cases} \frac{\partial p_1}{\partial x} = & j_{1y}B_{0z} + j_{1y}B_{1z} - j_{0z}B_{1y} - j_{1z}B_{1y} \\ \frac{\partial p_1}{\partial y} = & j_{1z}B_{0x} + j_{0z}B_{1x} + j_{1z}B_{1x} - j_{1x}B_{0z} \\ & -j_{0x}B_{1z} - j_{1x}B_{1z} \\ \frac{\partial p_1}{\partial z} = & j_{0x}B_{1y} + j_{1x}B_{1y} - j_{1y}B_{0x} - j_{1y}B_{1x} \end{cases} \tag{3}$$

If the magnetic field perturbation is approximated by a plane wave, the total field $\mathbf{B} = \mathbf{B_0} + \mathbf{B_1}$ becomes

$$\begin{cases} B_x = B_{0x} + B_{1x} = B_{0x} + A_1 e^{i\alpha x + i\gamma z} \\ B_y = B_{1y} = A_2 e^{i\alpha x + i\gamma z} \\ B_z = B_{0z} + B_{1z} = B_{0z} + A_3 e^{i\alpha x + i\gamma z} \end{cases} \tag{4}$$

where α and γ are the wave numbers along x and z, respectively, and $A_i = A_i(y)$ for $i = 1, ..., 5$. Substituting $\mathbf{B_1}(x, y, z)$ into equations (2) and (3) shows that the pressure must have a wave form as well, but it also includes the second harmonic term:

$$p_1 = A_4 e^{i\alpha x + i\gamma z} + A_5 e^{2i\alpha x + 2i\gamma z} \, . \tag{5}$$

Substituting the $\mathbf{B_1}$ field from equations (4) into equations (2), and that together with equations (1) and (5) into equations (3), we get a set of equations for $A_1 - A_4$:

$$\begin{cases} i\alpha A_1 + A_2' + i\gamma A_3 = 0 \\ i\gamma B_{0z} A_1 + B_{0x}' A_2 - i\alpha B_{0z} A_3 - i\alpha \mu_0 A_4 = 0 \\ -B_{0x}' A_1 - B_{0x} A_1' + i(\alpha B_{0x} + \gamma B_{0z}) A_2 \\ -B_{0z}' A_3 - B_{0z} A_3' - \mu_0 A_4' = 0 \\ -i\gamma B_{0x} A_1 + B_{0z}' A_2 + i\alpha B_{0x} A_3 - i\gamma \mu_0 A_4 = 0 \end{cases} \tag{6}$$

where the primes mark the derivative with respect to y. The second-order terms have been neglected causing the second harmonic term in p_1 (A_5) to vanish. Equations (6) can be solved to give A_2 as a function of α and γ:

$$A_2'' - \left[(\alpha^2 + \gamma^2) + \frac{\alpha B_{0x}'' + \gamma B_{0z}''}{\alpha B_{0x} + \gamma B_{0z}} \right] A_2 = 0 \, , \tag{7}$$

and thereafter A_1, A_3, A_4 as functions of α, γ and A_2.

Considering a current sheet in the x–z plane between $y = a$ and $y = -a$, we obtain an expression for $B_{0x}(y)$:

$$B_{0x} = \begin{cases} -\mu_0 j_0 a \, , & \text{when } y < -a \\ \mu_0 j_0 y \, , & \text{when } |y| \le a \\ \mu_0 j_0 a \, , & \text{when } y > a \end{cases} \tag{8}$$

If B_{0z} is assumed to be constant, equation (7) for A_2 becomes

$$A_2'' - k^2 A_2 = 0 \, , \tag{9}$$

where $k^2 = \alpha^2 + \gamma^2$. Then, A_2 is of the form

$$A_2 = \begin{cases} C_3 e^{ky} & , \text{when } y < -a \\ C_1 e^{ky} + C_2 e^{-ky} & , \text{when } |y| \le a \\ C_4 e^{-ky} & , \text{when } y > a \end{cases} \tag{10}$$

Rewriting equation (7) yields

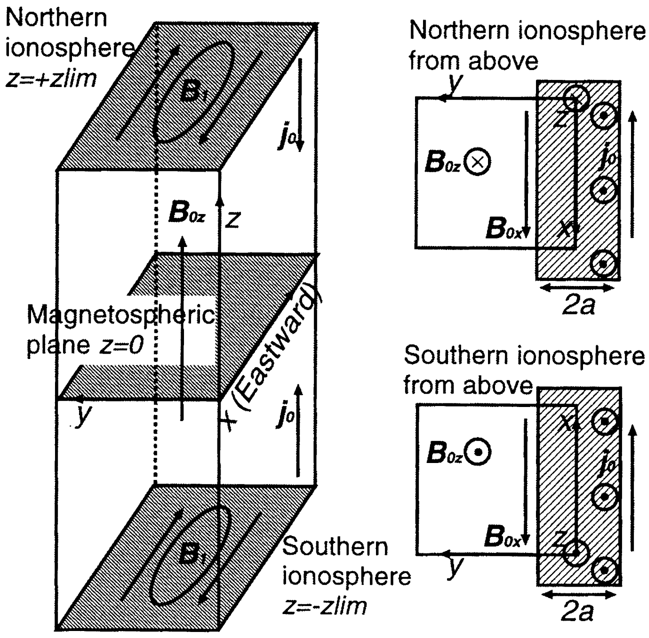

Figure 4. Coordinate system used in the model: x is eastward, y is earthward (southward in the Northern Hemisphere and northward in the Southern Hemisphere), and z along the magnetic field vector

$$(\alpha B_{0x}+\gamma B_{0z})(k^2A_2-A_2'') = -(\alpha B_{0x}''+\gamma B_{0z}'')A_2 \ . \quad (11)$$

Integrating the previous equation across the boundary $y = a$ gives

$$\begin{aligned} &\int_{a-\epsilon}^{a+\epsilon}(\alpha B_{0x} + \gamma B_{0z})k^2 A_2 dy \\ &- \int_{a-\epsilon}^{a+\epsilon}(\alpha B_{0x} + \gamma B_{0z})A_2'' dy \\ &= - \int_{a-\epsilon}^{a+\epsilon}(\alpha B_{0x}'' + \gamma B_{0z}'')A_2 dy \ , \end{aligned} \quad (12)$$

where ϵ is an infinitesimal parameter. Substituting A_2 from equation (10) to the first term on the left-hand side of equation (12), applying the partial integration, and finally taking the limit $\epsilon \to 0$ shows that this term vanishes. Partial integration of the two remaining terms of (12) yields

$$[(\alpha B_{0x} + \gamma B_{0z})A_2' - \alpha B_{0x}' A_2]_{a-\epsilon}^{a+\epsilon} = 0 \ . \quad (13)$$

Thus this expression is continuous across the boundary $y = +a$. The same applies to the other boundary ($y = -a$), too. Again, substituting A_2 from equation (10) into equation (13) at $y = \pm a$, we obtain a set of equations for C_1, C_2, C_3, and C_4. Eliminating C_2, C_3, and C_4 from these equations gives an expression

$$\{\alpha^2 \mu_0^2 j_0^2[(2ka-1)^2 - e^{-4ka}] - 4k^2\gamma^2 B_{0z}^2\}C_1 = 0 \ . \quad (14)$$

In the limit $\gamma^2 \ll \alpha^2$ and hence $\alpha^2/k^2 \approx 1$, we can solve equation (14) for the growth rate of the instability:

$$\gamma = \pm\sqrt{\frac{\mu^2 j_0^2}{4B_{0z}^2}[(2ka - 1)^2 - e^{-4ka}]} \ . \quad (15)$$

This is the extent of the theory published by *Hallinan* [1976]. More generally, we can solve equation (14) using $k^2 = \alpha^2 + \gamma^2$ to yield

$$\gamma^* = \pm\sqrt{\frac{B_{0xa}^{*2}k^{*2}[(2k^* - 1)^2 - e^{-4k^*}]}{B_{0xa}^{*2}[(2k^* - 1)^2 - e^{-4k^*}] + 4k^{*2}B_{0z}^{*2}}} \ , \quad (16)$$

where B_{0z} is assumed to be constant, $B_{0z}^* = B_{0z}/B_{0z} = 1$, $\mu_0 j_0 a = B_{0xa}$, $B_{0xa}^* = B_{0xa}/B_{0z}$, and $k^* = ka$. This can also be expressed by

$$\gamma^* = \pm\frac{Q}{R}k^* \ , \quad (17)$$

where

$$Q = \pm\sqrt{(2k^* - 1)^2 - e^{-4k^*}} \ ,$$

$$R = \pm\sqrt{Q^2 + \frac{4k^{*2}}{B_{0xa}^{*2}}} \ .$$

Finally, we continue the derivation to yield the complete solution for the magnetic field. Similarly to k^* and B_{0xa}^*, we also normalize all the other magnetic variables by the constant background B_{0z}, and all the lengths by the half width of the current sheet a. From now on, we use only these normalized (asterisked) variables:

$$\begin{aligned} k^{*2} &= \alpha^{*2} + \gamma^{*2} \ , && (18) \\ B_x^* &= B_{0x}^* + A_1^* e^{i\alpha^* x^* + i\gamma^* z^*} \ , && (19) \\ B_y^* &= A_2^* e^{i\alpha^* x^* + i\gamma^* z^*} \ , && (20) \\ B_z^* &= B_{0z}^* + A_3^* e^{i\alpha^* x^* + i\gamma^* z^*} \ , && (21) \\ C_2^* &= C_1^* e^{2k^*}[(2k^* - 1) \pm Q] \ , && (22) \\ C_3^* &= C_1^*\{1 + e^{4k^*}[(2k^* - 1) \pm Q]\} \ , && (23) \\ C_4^* &= C_1^* e^{2k^*}[2k^* \pm Q] \ , && (24) \end{aligned}$$

$$A_1^* = \begin{cases} \frac{i\alpha^*}{k^*}C_1^* e^{k^*y^*}\{1 + e^{4k^*}[(2k^* - 1) \pm Q]\}, \\ \text{when } y^* < -1 \\ \\ \frac{i\alpha^*}{k^*}C_1^*\{e^{k^*y^*} - e^{2k^*-k^*y^*}[(2k^* - 1) \pm Q]\} \\ + \frac{2i\gamma^{*2}C_1^*\{e^{k^*y^*} + e^{2k^*-k^*y^*}[(2k^*-1)\pm Q]\}}{\alpha^* k^*[2k^*y^* \pm Q]}, \\ \text{when } |y^*| \le 1 \\ \\ -\frac{i\alpha^*}{k^*}C_1^* e^{2k^*-k^*y^*}[2k^* \pm Q], \\ \text{when } y^* > 1 \end{cases} \quad (25)$$

$$A_2^* = \begin{cases} C_1^* e^{k^*y^*}\{1 + e^{4k^*}[(2k^* - 1) \pm Q]\}, \\ \text{when } y^* < -1 \\ \\ C_1^*\{e^{k^*y^*} - e^{2k^*-k^*y^*}[(2k^* - 1) \pm Q]\}, \\ \text{when } |y^*| \le 1 \\ \\ C_1^* e^{2k^*-k^*y^*}[2k^* \pm Q], \\ \text{when } y^* > 1 \end{cases} \quad (26)$$

$$A_3^* = \begin{cases} \frac{i\gamma^*}{k^*}C_1^* e^{k^*y^*}\{1 + e^{4k^*}[(2k^* - 1) \pm Q]\}, \\ \text{when } y^* < -1 \\ \\ \frac{i\gamma^*}{k^*}C_1^*\{e^{k^*y^*} - e^{2k^*-k^*y^*}[(2k^* - 1) \pm Q]\} \\ - \frac{2i\gamma^* C_1^*\{e^{k^*y^*} + e^{2k^*-k^*y^*}[(2k^*-1)\pm Q]\}}{k^*[2k^*y^* \pm Q]}, \\ \text{when } |y^*| \le 1 \\ \\ -\frac{i\gamma^*}{k^*}C_1^* e^{2k^*-k^*y^*}[2k^* \pm Q], \\ \text{when } y^* > 1 \end{cases} \quad (27)$$

3.2. Relationship of Auroral Spiral Model to Observations

3.2.1. Free parameters and the growth rate. We shall now show how the solution given above can give rise to an auroral spiral. For $\gamma^{*2} < 0$, the solution describes a helical twisting of magnetic field lines due to the spatially periodic perturbation of the equilibrium field-aligned current sheet. Let us now look at the signs of the growth rate of the instability γ^* in equation (17): If $k^{*2} > 0$ and $B_{0xa}^{*2} > 0$, then the only possibility for $\gamma^{*2} < 0$ (to get an exponential growth along the field line) is that $Q^2 < 0$ and $|Q^2| \le 4k^{*2}/B_{0xa}^{*2}$. Then k^* can be only in the range $0 < k^* < 0.64$ (if $B_{0xa}^* \le 1$). Then also α^* (see equation (18)) varies in approximately the same range, when $|\gamma^{*2}|$ is small. The sign of Q/R has to be chosen to give a growing mode of the instabil-

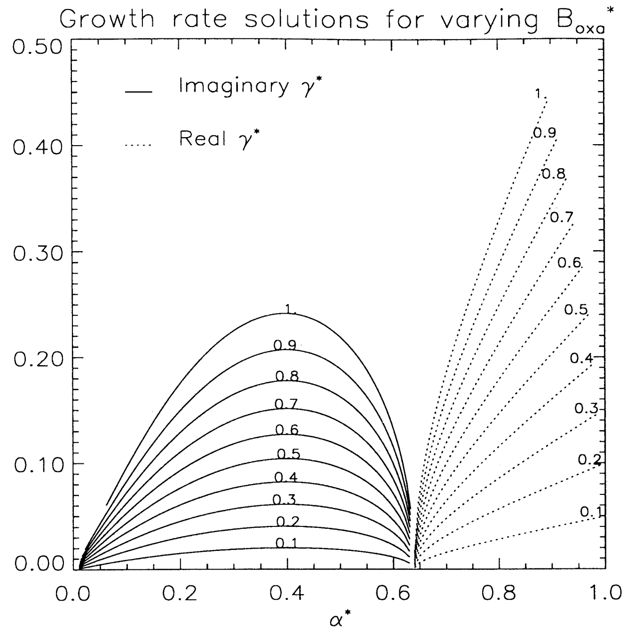

Figure 5. Variation of the growth rate γ^* as a function of the wave function in x direction, α^*, for various values of B^*_{0xa}.

ity from the equator to the ionosphere for both hemispheres, that is, negative for the Northern Hemisphere and positive for the Southern Hemisphere. The sign for Q appears also in expressions for the C and A variables, and there is no a priori physical knowledge on how the signs should be chosen. Using the same sign for Q in the expression for the C and A variables as is used for Q/R in the equation for γ^* produces smoother bending field lines than the other options. Thus this is the choice we use hereafter. The variation of γ^* as a function of α^* with different values of B^*_{0xa} is shown in Figure 5. The maximum of an imaginary γ^* (the fastest growth of the instability along z) is obtained when $\alpha^* = 0.4 \cong k^*$. The condition of maximum growth rate sets a value for the free parameter k^*. The two other free parameters in the model are B^*_{0xa} and C^*_1. B^*_{0xa} adjusts the strength and the direction of the current in the FAC sheet, and C^*_1 defines the intensity of the perturbation.

3.2.2. Spiral shape and interhemispheric symmetry. In order to relate the above discussion to auroral spirals, we shall assume that the field-aligned current sheet is a source of zero pitch angle precipitating particles which give rise to auroral emission in the ionospheric plane. If the precipitating particles are electrons, then this implies an upward FAC (away from the ionosphere), and hence the sign of B^*_{0xa} must be positive in the Northern Hemisphere and negative in the Southern Hemisphere.

To model the auroral spiral, we follow the paths of the zero pitch angle precipitating particles by taking a grid of points within the current sheet in the magnetospheric plane and tracing each point along its magnetic field line until it reaches the ionospheric plane. The resultant distribution of points delineates the auroral precipitation region in the northern and southern ionospheric planes and is shown by the colored regions in Plates 1b and 1d. The color coding represents the y coordinate of the current sheet field line in the magnetospheric plane, ranging from red at $y = +a$, through green/light blue at $y \sim 0$, to black at $y = -a$. Allowing for the distorted field of view of the ASC and the simplicity of the model, the spiral shape of the observed auroral spirals in Plates 1a and 1b is well reproduced by the model. The winding direction is also correct: counterclockwise in the Northern Hemisphere and clockwise in the Southern Hemisphere when viewed from above (i.e., from the $z = 0$ plane toward the planes $z =_{\text{zlim}}$ and $z = -z_{\text{lim}}$).

Examples of the single field lines corresponding to Plates 1b and 1d are shown in Figures 6 and 7. Note that the azimuthal magnetic field related to the current filament has the same sense of rotation in both hemispheres (counterclockwise, see $\mathbf{B_1}$ in Figure 4). However, in the Southern Hemisphere the particle trajectories are directed opposite to the magnetic field (not just in the z, but also in the x and y directions). Consequently, the counterclockwise perturbation field causes clockwise winding of the final structure. If the upward FAC sheet is replaced with a downward current sheet, that is, the sign of B^*_{0xa} is changed, the model produces a so-called black spiral [*Trondsen and Cogger,* 1997; *Kosch et al.,* 1998]. These structures have a winding direction opposite to that of the visible spirals.

3.2.3. Winding and unwinding of auroral spirals. The free parameter values used in Plates 1b and 1d were $B^*_{0xa} = 0.1$ in the Northern Hemisphere and $B^*_{0xa} = -0.1$ in the Southern Hemisphere, $C^*_1 = 0.01$ for a small perturbation, $k^* = 0.4$, and $z_{\text{lim}} = 120$. As can be seen from Figure 5, $k^* = 0.4$ was chosen to maximize the growth rate γ^*, and hence the amount of field line

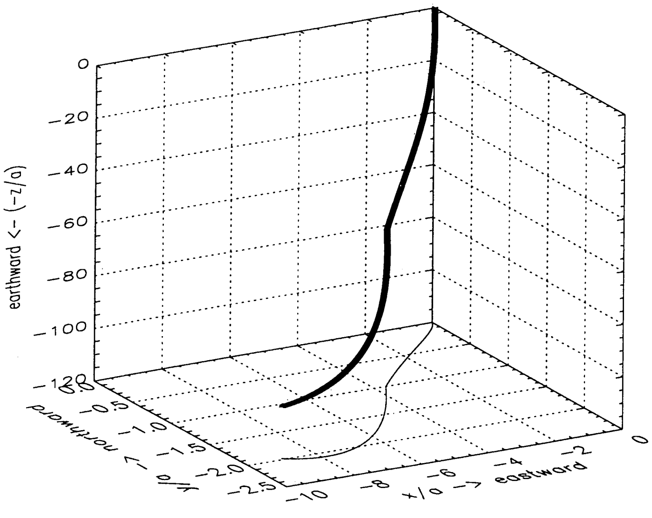

Figure 6. A single field line corresponding to the spiral in Plate 1b.

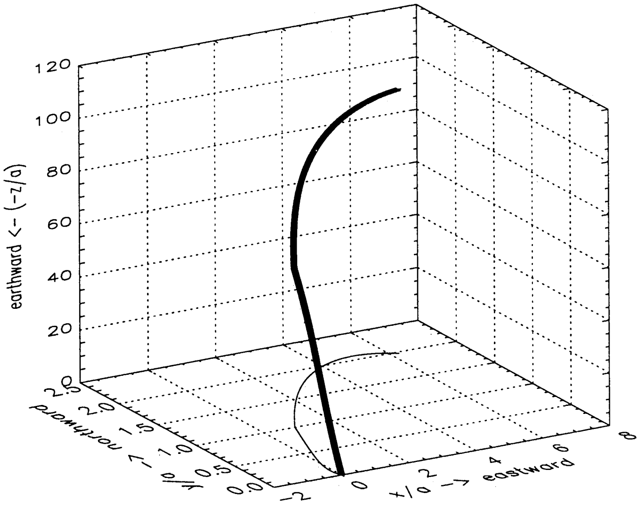

Figure 7. A single field line corresponding to the spiral in Plate 1d.

twisting over the distance $z_{\rm lim}$ and thus the amount of auroral spiral winding in the ionospheric plane. Figure 5 shows that increasing B^*_{0xa} also increases the growth rate γ^* and thus auroral spiral winding.

Increasing the perturbation $C^*_{\rm I}$ also causes the spiral winding to increase because the magnetic field perturbations are all proportional to $C^*_{\rm I}$. This may explain the observed relationship between auroral spiral intensity and amount of winding shown in Figure 2. The uppermost and lowermost panels in Figure 2 show a sequence of a model auroral spiral that winds and unwinds in a manner qualitatively similar to the auroral spiral seen in the ASC images of this figure. The winding and unwinding of the model spirals was achieved by varying the perturbation $C^*_{\rm I}$ between 0.001 and 0.01 in a quasi-periodic manner. Since the variation in $C^*_{\rm I}$ is proportional to the variation in FAC perturbation, we may then expect that the intensity of auroral precipitation would also vary as observed by the variation in the number of saturated pixels or the sum of relative intensities in the ASC images.

Strengthening the perturbation, that is increasing $C^*_{\rm I}$, causes the spiral to wind a given amount within a shorter distance along z^*. An interesting task is to try to resolve how different $C^*_{\rm I}$ values affect the distance along z^* ($z_{\rm lim}$) within which the spiral is completely wound. This can be done "empirically" by gradually lengthening field line tracings for a certain $C^*_{\rm I}$ value until a completely wound spiral (resembling the spirals in Plate 1) is achieved. The asterisks in Figure 8 show the results of this method (pairs of $C^*_{\rm I}$ and $z_{\rm lim}$). The task can also be resolved analytically. Equations (18)–(27) show that if $C^*_{\rm I}$ is increased by a factor p, the magnetic field solution remains the same if $\gamma^* z^*$ is multiplied by a factor q, where $q = 1 - \ln(p)/i\gamma^* z^*$. If we assume that $B^*_{0xa} = 0.1$, $k^* = 0.4$, and $C^*_{\rm I} = 0.01$, then the spiral is completely wound when $z^* = z_{\rm lim} = 120$. These values can be used to define first γ^*, and then p and q for different pairs of $C^*_{\rm I}$ and z^*. The solid line in Figure 8 shows this solution. The two different methods show the same overall behavior. The difficulty in defining when the spiral is completely wound, especially for large $C^*_{\rm I}$, causes the scatter in the empirically determined points. Because the magnetic field components are proportional to $C^*_{\rm I} e^{i\alpha^* x^*}$, changing the sign of $C^*_{\rm I}$ changes the proportionality to $C^*_{\rm I} e^{i\alpha^* x^* + \pi}$, and thus corresponds to a phase shift of one π in the x direction of the structure (cf. equations (19), (20), and (21)).

4. Discussion

4.1. Spatial Scales

As all the lengths in Hallinan's model are proportional to the half width a of the underlying auroral arc in the magnetosphere, it is difficult to define the spiral size in measurable units. This is especially true because determining the width of an auroral arc is not a straightforward task. The value of the model would increase remarkably if we were able to compare the sizes of the observed and modeled structures and see if there is a favorable spiral scale according to Hallinan's theory. Hallinan achieved the same ka value (0.4) for the maximum growth rate of the instability as our more general formulae yield. This value corresponds to $\lambda/2a \sim 8$, where λ is the interspiral separation. The observed values are in the range from 17 to 23 [*Davis and Hallinan,* 1976]. Hallinan explained this discrepancy by the change of the spatial scales in the mapping from the magnetosphere to the ionosphere. Nevertheless, as the model has a constant background field, it is difficult to estimate the exact mapping effects for the spiral dimensions. Consequently, we do not consider the observations of $\lambda/2a$ values as clear support of the model as *Davis and Hallinan* [1976] do.

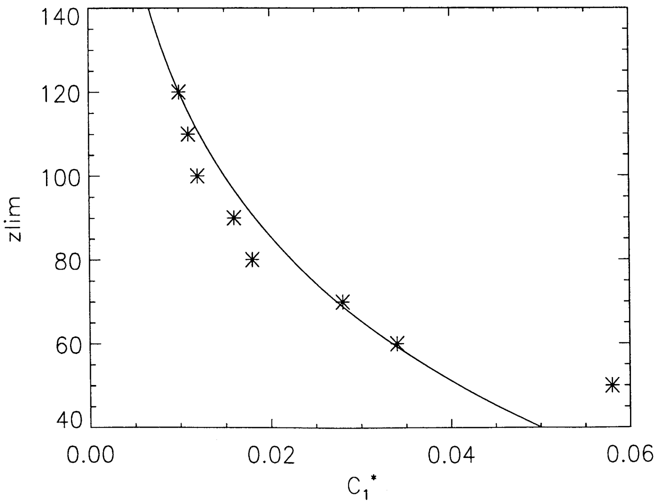

Figure 8. Observed dependence of a completely wound spiral on $C^*_{\rm I}$ and z/a, together with the log-law curve.

The mapping factor of the spatial scales in the near-Earth region can be estimated by a simple rule based on the dipole background field B_{0z} [*Borovsky*, 1993]:

$$W_{\mathrm{mag}} = W_{\mathrm{ion}}(\frac{r_{\mathrm{mag}}}{r_{\mathrm{ion}}})^{3/2}(\frac{4-3\sin^2\theta}{4-3r_{\mathrm{mag}}/r_{\mathrm{ion}}\sin^2\theta})^{1/2} , \quad (28)$$

where θ is the angle from the magnetic pole (magnetic colatitude), W_{mag} is the arc width in the magnetosphere, W_{ion} is arc width in the ionosphere, and r_{mag} and r_{ion} are the distances of the magnetosphere and the ionosphere from the dipole center, respectively. The distance r_{ion} is approximately the Earth's radius R_E. According to the model discussed here, the spiral is completely wound within a distance of about $120a$ (a is the half width of the arc) from the source region if the amplitude of the perturbation field is at least 1% of B_{0z}. By mapping arcs with W_{ion} 1–5 km to distances between 2–6 R_E, we get W_{mag} values of 3–160 km. If W_{mag} is assumed to be an upper limit for $2a$, the corresponding estimates for $120a$ vary from 150 km to 1.3 R_E. Consequently, the spirals wind up within relatively short distances. However, the assumption of the perturbation field intensity is not reasonable in the near-Earth region, where the background field is strong. As Figure 8 shows, a small decrease in the perturbation amplitude causes an exponential increase in the winding distance. An upgraded Hallinan-type model with a more realistic background field configuration is needed before we can resolve if the distance from the acceleration region altitudes to the ionosphere is long enough for spirals to wind. Further challenges for future studies would be solving the complete set of equations (6) without neglecting the second-order terms, which would also give a new insight into the theory, either new or the same solutions. Including also the second harmonic term in the expression for the pressure in equation (5) would probably lead to a solution of turbulence or maybe explain the auroral breakup.

4.2. Spirals and Westward Traveling Surges

The relationship between spirals and westward traveling surges (WTS) needs further examination. These structures have similar scale sizes, are accompanied by FACs, and cause similar variations in the ground magnetic field [*Davis and Hallinan*, 1976; *Opgenoorth*, 1983]. However, their temporal development is different: At the western edge of a WTS, auroral structures move in the same direction as the surrounding plasma flow (clockwise at the ionospheric foot point of an upward FAC in the Northern Hemisphere) [*Nakamura et al.,* 1993], while in a case of a spiral the structures seem to move in the direction opposite to the anticipated plasma flow. This suggests that the magnetospheric processes controlling these two phenomena are different, and a WTS cannot be considered as a large spiral.

4.3. Comparison to More Recent Models of Auroral Vortices

Samson et al. [1996] reported on auroral arcs and large-scale vortices produced by ultralow frequency (periods of about 4–16 min) field line resonances (FLR). FLRs often occur in the equatorward part of the auroral oval, where the field lines are nearly dipolar. In the resonance the magnetic field antinodes (electric and velocity field nodes) take place in the ionospheric ends, and the nodes (electric and velocity field antinodes) appear in the equatorial magnetosphere. Thus the plasma flow in the equatorial region experiences a strong radial shear, which can be unstable to KHI and produce vortex-like structures. Shear Alfvén waves (SAW) driven by the magnetospheric vortex propagate to the ionospheres, leading to the formation of plasma flow and auroral structures with the scale size of the order of hundreds of kilometers. The model predicts such vortices with both rotational senses. The equal probability of observing both winding directions does not support the observations of the systematic counterclockwise (clockwise) winding of the northern (southern) hemispheric spirals.

A more recent model by *Voronkov et al.* [1999] concentrates on the nonlinear evolution of the KHI in the FLR, but in three-dimensional dipole magnetic field configuration. This geometry allows the interaction of processes between different altitude levels along the magnetic field lines, which introduces some differences in the field-aligned growth rate of the instability. In general, however, the results turned out to be quite similar to the predictions of the two-dimensional theories [e.g., *Samson et al.,* 1996; *Voronkov et al.,* 1997b]. Compared to the observations and simulations by Samson et al., the structures described by this model are smaller (scale sizes of the order of 10 km and growth times of 100–200 s). Furthermore, the model predicted clockwise winding of the spirals in the Northern Hemisphere, which together with the size suggests that the vortices are rather curls than spirals, as originally argued for the KHI by *Hallinan and Davis* [1970].

Numerical modeling by *Voronkov et al.* [1997a] established a coupling between the shear flow and the ballooning instability. On the basis of these calculations, the simulations by *Voronkov et al.* [2000] suggested that the shear flow ballooning instability in the near-Earth plasma sheet could also be a possible mechanism of large-vortex formation during substorms and pseudobreakups. The KHI in the FLR alone cannot be responsible for the large-scale vortex formation, because the growth of the KHI is limited by the width of the shear flow channel. However, when the KHI grows toward the saturation, it can trigger a ballooning instability. The coupling between the two instabilities enables the vortex to continue growing and expand outside the region of the initial shear flow. At the saturation stage, the shape of the auroral vortex changes to a mushroomlooking structure and the spiral-like morphology disappears. Consequently, this model may not be applicable to the majority of our events, which have high rotational symmetry and occasionally even reversible behavior.

In summary, it seems likely that the KHI of a (FLR) velocity shear is responsible for the generation of small-scale auroral curls [*Hallinan and Davis,* 1970; *Voronkov et al.,* 1999], whereas large-scale spirals are generated either by the mathematically analogous but physically distinct magnetic shear instability [*Hallinan,* 1976], KHI in FLRs [*Samson et al.,* 1996], or ballooning instability in FLRs [*Voronkov et al.,* 2000]. However, the KHI may coexist with the magnetic shear instability and indeed auroral curls are observed to coexist with auroral spirals [*Hallinan and Davis,* 1970]. Thus the static spiral model needs to be improved to incorporate many of the SAW effects included in the KHI models. In particular, the inhomogeneous background magnetic field and ionospheric conductivity boundary conditions should be considered and time dependence should be included since changes in spiral winding will be communicated along the magnetic field by shear Alfvén waves whose transit times from the magnetospheric equator to the ionospheres is comparable to the spiral winding time. Nevertheless, despite its simplifications, the Hallinan model is remarkably successful in describing the essential morphology of auroral spirals.

5. Conclusions

This study presents for the first time in the literature a unique ASC data set of 216 auroral spirals: comparable recordings from the both hemispheres and also observations of the scale sizes of southern hemispheric spirals. These data show the systematic winding directions of the spirals: counterclockwise (clockwise) in the Northern (Southern) Hemisphere. We have also been able to reliably relate the brightness of the aurora to the winding and unwinding processes of the spirals. When the spiral is winding (unwinding), the brightness increases (decreases), and the auroral precipitation as well as the accompanying FAC increases (decreases). In addition, our observations show that spirals wind in the direction opposite to the anticipated plasma flow (clockwise around an upward FAC).

The simple spiral model by *Hallinan* [1976] describes surprisingly well the observed winding directions of the auroral spirals. That is why we wanted to discuss more about some of the interesting details (e.g., free parameters) in the derivation of the model, which were not commented on in the original paper. The model assumes a FAC filament to extend from the magnetosphere to the ionosphere. In reality, currents are field aligned only near the ionospheric end of the flux tube where the plasma β is very low, the thermal pressure gradient is negligible, and the force balance reduces to $\mathbf{J} \times \mathbf{B} = 0$. The approximate calculation by *Samson et al.* [1996] suggests that the field line twisting may remain incomplete only if the process takes place in this low-β regime. Resolving this issue, as well as defining the theoretical predictions of the spiral sizes, more rigorously would need improving Hallinan's model with a more realistic background magnetic field.

Acknowledgments.
The work by N. P. was supported by the Finnish Graduate School in Astronomy and Space Physics. The MIRACLE network is operated as an international collaboration under the leadership of the Finnish Meteorological Institute. M. Syrjäsuo wrote the software for mapping the TULA images. Our thanks go to Neil Cobbett, James Fox, David Maxfield, Mike Rose and all members of the British Antarctic Survey who have helped to maintain and operate the TULA all-sky camera experiment at Halley, Antarctica.

Michel Blanc thanks Igor Voronkov and Michael Kosch for their assistance in evaluating this paper.

References

Borovsky, J., Auroral arc thicknesses as predicted by various theories, *J. Geophys. Res., 98*, 6101–6138, 1993.

Davis, T. N., and T. J. Hallinan, Auroral spirals, 1, Observations, *J. Geophys. Res., 81,* 3953–3958, 1976.

Hallinan, T. J., Auroral spirals, 2, Theory, *J. Geophys. Res., 81,* 3959–3965, 1976.

Hallinan, T. J., and T. N. Davis, Small-scale auroral arc distortions, *Planet. Space Sci., 18,* 1735–1744, 1970.

Kosch, M. J., M. W. J. Scourfield, and E. Nielsen, A self-consistent explanation for a plasma flow vortex associated with the brightening of an auroral arc, *J. Geophys. Res., 103,* 29,383–29,391, 1998.

Moen, J., P. E. Sandholt, M. Lockwood, A. Egeland, and K. Fukui, Multiple, discrete arcs on sunward convecting field lines in the 14–15 MLT region, *J. Geophys. Res., 99,* 6113–6123, 1994.

Nakamura, R., T. Oguti, T. Yamamoto, and S. Kokubun, Equatorward and poleward expansion of the auroras during auroral substorms, *J. Geophys. Res., 98,* 5743–5759, 1993.

Oguti, T., Rotational deformations and related drift motions of auroral arcs, *J. Geophys. Res., 79,* 3861–3865, 1974.

Opgenoorth, H. J., R. J. Pellinen, W. Baumjohann, E. Nielsen, G. Marklund, and L. Eliasson, Three-dimensional current flow and particle precipitation in a westward travelling surge (observed during the barium-GEOS rocket experiment), *J. Geophys. Res., 88,* 3138–3152, 1983.

Partamies, N., K. Kauristie, T. I. Pulkkinen, and M. Brittnacher, Statistical study on auroral spirals, *J. Geophys. Res.,* in press, 2001.

Samson, J. C., L. L. Cogger, and Q. Pao, Observations of field line resonances, auroral arcs, and auroral vortex structures, *J. Geophys. Res., 101,* 17,373–17,383, 1996.

Syrjäsuo, M.T., et al., Observations of substorm electrodynamics using the MIRACLE network, *Proc. Int. Conf. Substorms 4th, 238,* 111–114, 1998.

Trondsen, T., and L. L. Cogger, High-resolution television observations of black aurora, *J. Geophys. Res., 102,* 363–378, 1997.

Trondsen, T., and L. L. Cogger, A survey of small-scale spatially periodic distortions of auroral forms, *J. Geophys. Res., 103,* 9405–9415, 1998.

Voronkov, I., R. Rankin, V.T. Tikhonchuk, and J.C. Samson, Non-linear shear Alfvén resonances in a dipolar magnetic field, *J. Geophys. Res., 102,* 27,137–27,143, 1997a.

Voronkov, I., R. Rankin, P. Frycz, V.T. Tikhonchuk, and J.C. Samson, Coupling of shear flow and pressure gradient instabilities, *J. Geophys. Res., 102*, 9639–9650, 1997b.

Voronkov, I., R. Rankin, J.C. Samson, and V.T. Tikhonchuk, Shear flow instability in the dipolar magnetosphere, *J. Geophys. Res., 104*, 17,323–17,334, 1999.

Voronkov, I., E. F. Donovan, B. J. Jackel, and J.C. Samson, Large-scale vortex dynamics in the evening and midnight auroral zone: Observations and simulations *J. Geophys. Res., 105*, 18,505–18,518, 2000.

M.P. Freeman, British Antarctic Survey, Madingley Road, Cambridge, CB3 0ET, UK. (MPF@pcmail.nercbas.ac.uk)

K. Kauristie and N. Partamies, Finnish Meteorological Institute, Geophysical Research, P.O.Box 503, FIN-00101 Helsinki, Finland. (kirsti.kauristie@fmi.fi; noora.partamies@fmi.fi)

(Received February 19, 2001; revised May 10, 2001; accepted June 12, 2001.)